



Preparation and enhanced visible-light photocatalytic activity of silver deposited graphitic carbon nitride plasmonic photocatalyst



Yuxin Yang^a, Yingna Guo^b, Fangyuan Liu^c, Xing Yuan^{a,*}, Yihang Guo^{b,**}, Shengqu Zhang^b, Wan Guo^b, Mingxin Huo^a

^a State Environmental Protection Key Laboratory of Wetland Ecology and Vegetation Restoration, School of Environment, Northeast Normal University, Changchun 130024, PR China

^b School of Chemistry, Northeast Normal University, Changchun 130024, PR China

^c College of Chemistry, Jilin University, Changchun 130012, PR China

ARTICLE INFO

Article history:

Received 31 March 2013

Received in revised form 8 June 2013

Accepted 21 June 2013

Available online 1 July 2013

Keywords:

Graphitic carbon nitride

Noble metal

Heterostructure

Plasmonic photocatalysis

Organic pollutant

ABSTRACT

A series of silver deposited g-C₃N₄ (Ag/g-C₃N₄) plasmonic photocatalysts with Ag loading from 0.1 to 5 wt% are prepared by thermal polymerization of urea precursor combined with the photodeposition method. The phase and chemical structure, electronic and optical properties as well as morphologies of Ag/g-C₃N₄ heterostructures are well-characterized. Subsequently, the photocatalytic activity of Ag/g-C₃N₄ is evaluated by the degradation of methyl orange (MO) and *p*-nitrophenol (PNP) under visible-light irradiation. The enhanced photocatalytic activity of Ag/g-C₃N₄ compared with g-C₃N₄ itself is obtained and explained in terms of the efficient visible-light utilization efficiency due to the SPR absorption of silver nanoparticles as well as fast generation, separation and transportation of the photogenerated carriers, evidenced by photoelectrochemical tests, photoluminescence measurements and free radical and hole scavenging experiments. Finally, the reusability of the catalyst is evaluated by five consecutive catalytic runs.

© 2013 Elsevier B.V. All rights reserved.

1. Introduction

The growing concerns about environmental and energy crises have stimulated intense research on solar energy utilization [1]. In the field of the elimination of organic pollutants, solar photocatalysis by semiconductors has emerged as one of the most promising technologies [2–5]. Nevertheless, wide bandgap and low quantum efficiency are still the “bottleneck” of the photocatalysts to meet the requirement of practical applications. For example, the most common TiO₂ is not an ideal photocatalyst because it performs rather poorly in the processes associated with solar photocatalysis. As a result, it is an urgent issue to search for efficient sunlight- or visible-light-driven photocatalysts. For this purpose, the modified TiO₂ and TiO₂-alternative photocatalysts have been developed [6–17]. However, it still remains a challenge to design stable photocatalysts that are abundant and facile preparation besides high visible-light efficiency.

In the search for robust and stable visible-light-driven photocatalysts, a polymeric semiconductor, graphitic carbon nitride (g-C₃N₄), has recently attracted a great deal of interest in photocatalytic applications. The heptazine ring structure and high degree of condensation make metal-free g-C₃N₄ possess many advantages such as good chemical stability as well as an appealing electronic structure with a medium-bandgap (2.7 eV). In addition, g-C₃N₄ is abundant and easily-synthesized *via* one-step polymerization of the cheap feedstocks like cyanamide [18,19], dicyandiamide [20–22], melamine [23–25], thiourea [20,26] and urea [20,27–29]. These unique properties make g-C₃N₄ a promising candidate for applications in solar photocatalysis. However, metal-free g-C₃N₄ suffers from disadvantages such as rapid recombination of the photogenerated electrons (e_{CB}[−]) and holes (h_{VB}⁺), low visible-light utilization efficiency and small BET surface area [18–26]. Accordingly, the development of reliable and facile strategies to fabricate the modified g-C₃N₄-based photocatalysts with unique physicochemical properties and photocatalytic performances is of growing interests. For this purpose, g-C₃N₄-based heterostructured photocatalysts such as g-C₃N₄/ZnO [30,31], g-C₃N₄/Fe₂O₃ [32], g-C₃N₄/ZnWO₄ [33], g-C₃N₄/Bi₂WO₆ [34], g-C₃N₄/BiOBr [35], g-C₃N₄/SmVO₄ [36] and g-C₃N₄/AgX (X=Br, I) [37] have been constructed. Among these materials, the conduction band (CB) of g-C₃N₄ (N 2p orbitals) is more negative than that of the coupled

* Corresponding author. Tel.: +86 431 85099561.

** Corresponding author. Tel.: +86 431 85098705; fax: +86 431 85098705.

E-mail addresses: yuanx@nenu.edu.cn (X. Yuan), guoyh@nenu.edu.cn (Y. Guo).

semiconductor, accordingly, the photoexcited e_{CB}^- generated on g-C₃N₄ or both components are effectively collected in the CB of the coupled semiconductor; meanwhile, the photoexcited h_{VB}^+ are effectively collected in the valence band (VB) of g-C₃N₄ (C 2p orbitals) since VB of g-C₃N₄ is more negative than that of the coupled semiconductor. The above procedures facilitate the efficient separation of the photogenerated carriers, leading to the enhanced photocatalytic activity compared with g-C₃N₄ itself. However, the reducibility of e_{CB}^- decreases obviously owing to the transportation of e_{CB}^- from the CB of g-C₃N₄ to that of the coupled semiconductor, giving a negative influence on the photocatalytic activity of g-C₃N₄/semiconductor. For example, under the visible-light irradiation of the heterostructured g-C₃N₄/BiOBr photocatalyst, the e_{CB}^- are injected into the CB of BiOBr (0.3 V vs. NHE) from that of g-C₃N₄ (−1.3 V vs. NHE) [18]. Owing to much positive CB edge of BiOBr compared with the standard redox potential of O₂/•O₂[−] (−0.046 V vs. NHE), the number of the generated superoxide radicals (•O₂[−]) decreases, which limits the enhancement of the photocatalytic activity of g-C₃N₄/BiOBr.

Herein, a series of silver deposited g-C₃N₄ heterostructures (Ag/g-C₃N₄) are prepared by thermal polymerization of urea precursor combined with photodeposition. Owing to utilization of the plasmonic nanostructure as the sensitizer for g-C₃N₄, as-prepared Ag/g-C₃N₄ are expected to improve the visible-light photocatalytic activity of g-C₃N₄-based materials significantly [38]. On the one hand, the surface plasmon resonance (SPR) effect of silver nanoparticle causes the intense local electromagnetic fields, which can speed the formation rate of h_{VB}^+ and e_{CB}^- within g-C₃N₄ [39]. Additionally, the favorable Fermi level of silver facilitates the separation of e_{CB}^- and h_{VB}^+ , which in turn enhances the quantum efficiency of g-C₃N₄ [40]. Moreover, the transferred e_{CB}^- shift the Fermi level to more negative potential, and thereby keeping the reducibility of e_{CB}^- in the Fermi level close to that in the CB of g-C₃N₄ [41]. On the other hand, the efficient utilization of sunlight can be realized due to SPR absorption in the visible-light region as well as UV light response of the interband transition of silver nanoparticles.

The phase and chemical structure, optical absorption properties as well as morphologies of Ag/g-C₃N₄ are well characterized, and the visible-light photocatalytic activity of Ag/g-C₃N₄ is evaluated by the degradation of two typical organic pollutants, methyl orange (MO) and *p*-nitrophenol (PNP). Meanwhile, the separation and transportation of the photogenerated carriers in the visible-light-irradiating Ag/g-C₃N₄ system is studied by photoluminescence (PL) spectroscopy measurements and photoelectrochemistry experiments, and the active species generated during the process of photodegradation are investigated by free radical and hole scavenging experiments. On the basis of the above results, mechanism of visible-light photocatalytic degradation of aqueous organic pollutants over Ag/g-C₃N₄ plasmonic photocatalyst is revealed, which is one of the most important issues for the TiO₂-alternative photocatalysts but is seldom studied up till now.

2. Experimental

2.1. Catalyst preparation

2.1.1. Graphitic C₃N₄

Urea (50 g) was put into an alumina crucible with a cover under ambient pressure in air, and then the crucible was heated in a muffle furnace to 250 °C for 1 h, 350 °C for 2 h and a final temperature 550 °C for 2 h at a heating rate of 2 °C min^{−1}. The yielded yellow powder was washed with nitric acid (0.1 mol L^{−1}) and distilled water to remove any residual alkaline species (e.g. ammonia)

adsorbed on the surface of the product, and then the product was dried at 80 °C for 12 h.

2.1.2. Ag deposited g-C₃N₄

As-prepared g-C₃N₄ powder (0.7 g) was dispersed into an aqueous AgNO₃ solution (90 mL) with the concentration of 0.08, 0.4, 0.8, 1.6, and 4 mmol L^{−1}, respectively, to obtain Ag deposited g-C₃N₄ materials with various Ag loadings (0.1, 0.5, 1, 2, and 5 wt%). The resulting suspension was irradiated under a 300 W Xe lamp (PLS-SXE300, Beijing Trusttech Co., Ltd.) for 2 h. The separated powder was washed with distilled water to remove the adsorbed Ag⁺ ions, and then the product was dried at 80 °C for 12 h. The products are denoted as Ag(*x*)/g-C₃N₄, where *x* represents Ag deposited level (wt%) in the products.

2.2. Catalyst characterization

Powder X-ray diffraction (XRD) patterns were obtained on a Japan Rigaku D/max 2000 X-ray diffractometer (Cu Kα, λ = 1.5418 Å). Fourier transform infrared (FT-IR) spectra were recorded on a Nicolet Magna 560 IR spectrophotometer. X-ray photoelectron spectroscopy (XPS) was performed on a VG-ADES 400 instrument with Mg K-ADES source. Transmission electron microscope (TEM) was recorded on a JEM-2100F high resolution transmission electron microscope at an accelerating voltage of 200 kV. Nitrogen porosimetry measurement was performed on a Micromeritics ASAP 2020M surface area and porosity analyzer. UV–vis diffuse reflectance spectra (UV–vis/DRS) were recorded on a Cary 500 UV–vis–NIR spectrometer. PL of the samples was obtained using a Varian Cary Eclipse spectrometer.

2.3. Photocatalytic tests

The adsorption and photocatalytic activity of as-prepared photocatalysts were evaluated by the degradation of MO and PNP under visible-light irradiation by a 300 W Xe lamp with an IR cut filter to remove IR irradiation from 680 nm to 1100 nm and a 400 nm cut filter to remove the UV irradiation. For all adsorption and photocatalysis experiments, 100 mL of aqueous MO or PNP solution with the initial concentration of 10 mg L^{−1} was used, and the catalyst amount was 100 mg. All experiments were performed in a self-made quartz photoreactor fitted with a circulation water system to maintain a constant temperature. Prior to irradiation, the adsorption–desorption equilibrium between the target compound and the catalyst was monitored by the determination of the concentrations of the target compound at a certain time interval. During the photocatalytic tests, fixed amounts of the reaction solution were taken out at given time intervals, followed by centrifugation to remove the photocatalyst completely. The concentrations of MO during the degradation procedures were determined by a Cary 60 UV–vis–NIR spectrometer at λ = 464 nm, and the concentrations of PNP were determined at λ = 317 nm and a Agilent 1200 high performance liquid chromatography: C18 column, UV detector (λ = 320 nm) and methanol/water (60/40, v/v) was used as a mobile phase at a flow rate of 1.0 mL min^{−1}. Final products such as NO₃[−] and SO₄^{2−} ions were analyzed by a Metrohm 881 Compact ion chromatography (IC) equipped with a Metrosep A SUPP 4 anion column and conductivity detector. Na₂CO₃ (1.8 mmol L^{−1}) and NaHCO₃ (0.17 mmol L^{−1}) were used as the mobile phase, and the detection limit of NO₃[−] and SO₄^{2−} is lower than 0.05 mg L^{−1}.

2.4. Photocurrent (PC) measurements

The working electrode was prepared on the rectangle titanium (Ti) sheets (size 10 mm × 50 mm, thickness 140 μm, purity > 99.6%), which was cleaned by sonication in water and alcohol for 10 min,

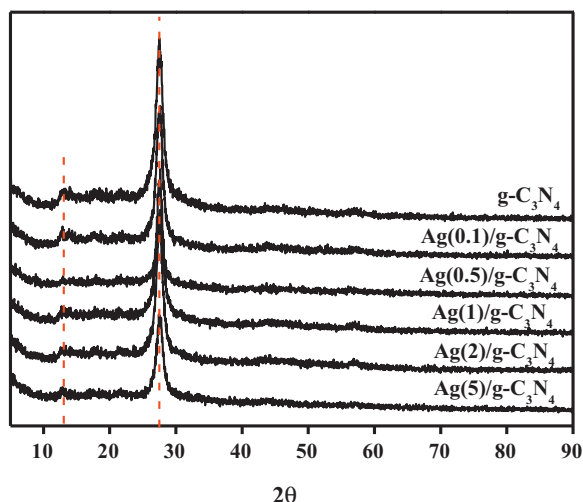


Fig. 1. XRD patterns of g-C₃N₄ and Ag/g-C₃N₄ materials.

respectively. The cleaned Ti sheets were chemically etched in a mixture of HF, HNO₃ and H₂O for 30 s (HF:HNO₃:H₂O = 1:4:5; v/v/v) followed by rinsing with distilled water and kept in alcohol. The catalyst powder (10 mg) was mixed with alcohol (2 mL) under sonication for 30 min to get slurry. The obtained slurry was used for spin-coating on the Ti sheet at an initial spin rate of 500 rpm for 9 s and then 2000 rpm for 10 s. After air drying, the prepared working electrode was heated at 60 °C for 6 h in air to improve the adhesion of the catalyst. The cooled Ti sheets were washed with water for three times. Finally, the sheets were dried at 60 °C for 24 h.

Photocurrent measurements were carried out using the conventional three electrode setup connected to an electrochemical station (CHI 630E, Shanghai Chenhua, China). In this electrochemical system, the prepared catalyst/Ti sheet was used as the working electrode; a Pt wire was used as the counter electrode and a Ag/AgCl electrode (saturated KCl) was used as the reference electrode. The electrolyte was 0.01 mol L⁻¹ Na₂SO₄ aqueous solution (100 mL). A 300 W Xe lamp served as a light source. The measurements were carried out at a constant potential of +1.0 V to the working electrode.

3. Results and discussion

3.1. Characterization

3.1.1. Structural information

Facile preparation of heterostructured Ag/g-C₃N₄ photocatalysts is realized by a reproducible polymerization–photodeposition strategy. The structural information of as-prepared Ag/g-C₃N₄ is provided by XRD, FT-IR and XPS measurements.

XRD analysis is used to investigate the phase structure of the Ag/g-C₃N₄ photocatalysts, and the graphitic stacking structure for all tested Ag/g-C₃N₄ materials is confirmed by the result shown in Fig. 1. The typical (002) interlayer-stacking peak at 27.5° corresponds to an interlayer distance of $d = 0.33$ nm for g-C₃N₄, while the peak at 13.1° represents in-plane structural packing motif with a period of 0.675 nm [27,42]. The XRD result also indicates that the diffraction intensity of the peak at 27.5° becomes weaker when the doping level of Ag reaches to 5 wt%; additionally, diffraction peaks related to the metallic Ag are hardly found, which may be due to the low doping levels and high dispersion of Ag clusters in Ag/g-C₃N₄ heterostructures.

FT-IR spectra can provide plentiful structural information concerning about g-C₃N₄ (see Fig. 2). For pure g-C₃N₄, a series of peaks found in the range from 1639 to 1208 cm⁻¹ attributes to the

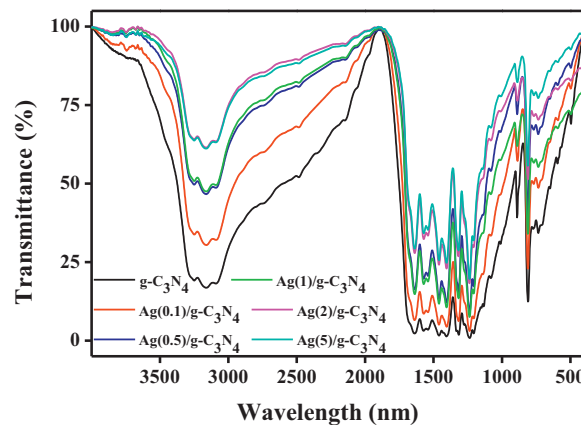


Fig. 2. FT-IR spectra of g-C₃N₄ and Ag/g-C₃N₄ materials.

typical stretching modes of CN heterocycles, while the sharp peak at 810 cm⁻¹ is assigned to the bending vibration of heptazine rings, revealing that the local structure of the obtained g-C₃N₄ is composed of heptazine units. The broad absorption band located in the range from 3300 to 3000 cm⁻¹ is originated from the stretching vibration of N–H bonds, associated with uncondensed amino groups [24,42,43]. After the deposition of metallic silver particles on the surface of g-C₃N₄, all characteristic vibrational peaks related to g-C₃N₄ can also be found in the Ag/g-C₃N₄ materials, suggesting that the structural integrity of g-C₃N₄ remains intact after the photodeposition. From the result it also can be seen that the IR absorption peaks of N–H bonds decrease gradually with the increase of Ag doping from 0.1 to 5 wt%. This is due to the fact that Ag⁺ can be anchored on the amino groups by complexation and redox [44], and subsequently photoreduced to Ag⁰ during the process of photodeposition. Therefore, the Ag nanoparticles grow around the amino groups and interfere with the stretching vibration of N–H bonds.

The high-resolution XPS surface probe technique can further confirm the local structure of the g-C₃N₄ and the metallic nature of deposited Ag (Fig. 3). Fig. 3a shows the XPS of Ag(2)/g-C₃N₄ in the C 1s binding energy regions, and three peaks centering at 284.6, 286.5 and 287.6 eV are found. These peaks are assigned to sp² C atoms bonded to N in an aromatic ring (N=C=N), sp³ hybridized C atoms (C–(N)₃), and the pure graphitic sites in a CN matrix, respectively [28,45]. Fig. 3b shows the XPS of Ag(2)/g-C₃N₄ in the N 1s binding energy regions, and the spectrum can be fitted into three peaks. The peak at 397.9 eV is assigned to sp² hybridized aromatic nitrogen atoms bonded to carbon atoms (C=N=C). The peak at 399.4 eV relates to either tertiary nitrogen N–(C)₃ groups linking structural motif (C₆N₇) or amino groups carrying hydrogen ((C)₂–N–H) in connection with structural defects and incomplete condensation. A weak peak at 400.2 eV corresponds to nitrogen atoms bonded three carbon atoms in the aromatic cycles [20]. Fig. 3c presents the XPS of Ag(2)/g-C₃N₄ in the Ag 3d binding energy regions, indicating that silver in the Ag(2)/g-C₃N₄ is of metallic nature with Ag 3d_{5/2} and Ag 3d_{3/2} binding energy of 367.4 eV and 373.4 eV and spin energy separation of 6.0 eV [13].

3.1.2. Textural property

The textural property of as-prepared Ag/g-C₃N₄ materials is characterized by nitrogen gas porosimetry measurement. The obtained sorption isotherms and BJH pore-size distribution curves are shown in Fig. 4. All tested g-C₃N₄-based materials exhibit type IV isotherms with H3 hysteresis loops, regardless of Ag doping levels, indicating the mesoporosity of the materials. The pore-size distribution curves clearly show that the g-C₃N₄-based materials exhibit two kind of mesopores centered at 3.7 and 33.0 nm, respectively (Fig. 4b). The formation of smaller pores are attributed to the

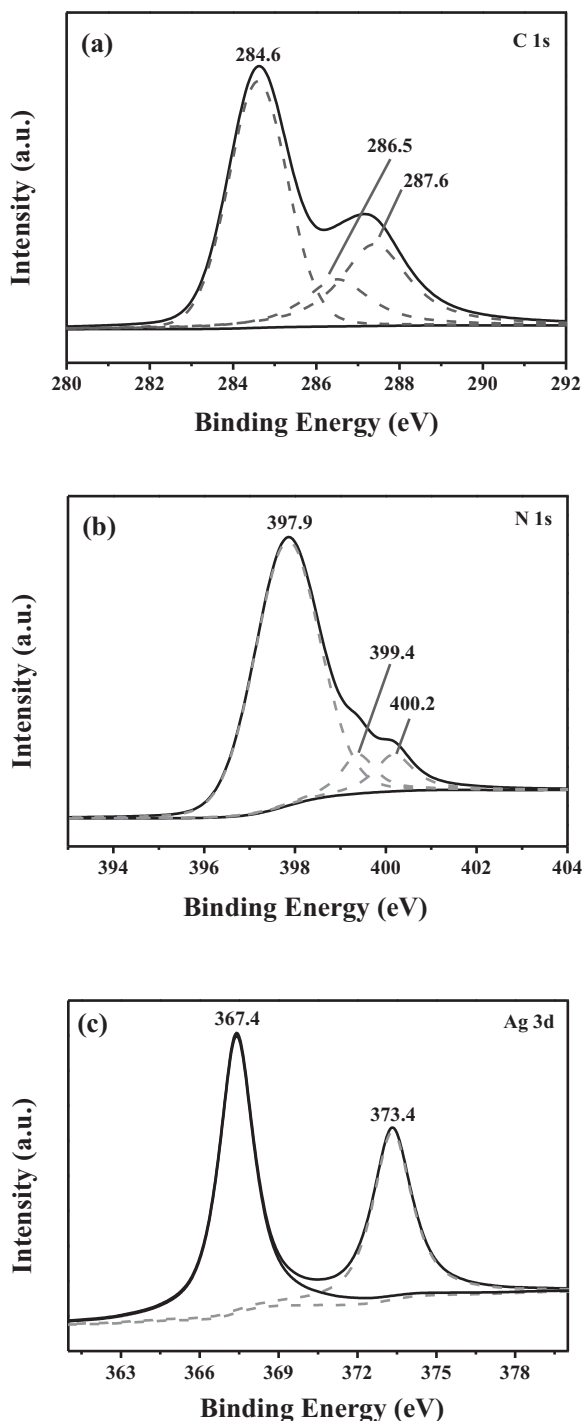


Fig. 3. High-resolution XPS of Ag(2)/g-C₃N₄ in the (a) C 1s, (b) N 1s and (c) Ag 3d binding energy regions.

released NH₃ and CO₂ that act as soft-templates during the course of urea polymerization [20]. The larger pores are produced due to the platelet-like morphology of g-C₃N₄. Moreover, due to the excellent porous structure, urea-derived g-C₃N₄ possesses much larger BET surface area (71 m² g⁻¹) compared with g-C₃N₄ prepared by other precursors (e.g., cyanamide, dicyandiamide and melamine) [20]. After the deposition of silver particles on the surface of g-C₃N₄, the BET surface areas of Ag/g-C₃N₄ materials decrease slightly, indicating that the mesoporosity of g-C₃N₄ remains intact. For example, the BET surface areas of Ag(0.1)/g-C₃N₄, Ag(0.5)/g-C₃N₄,

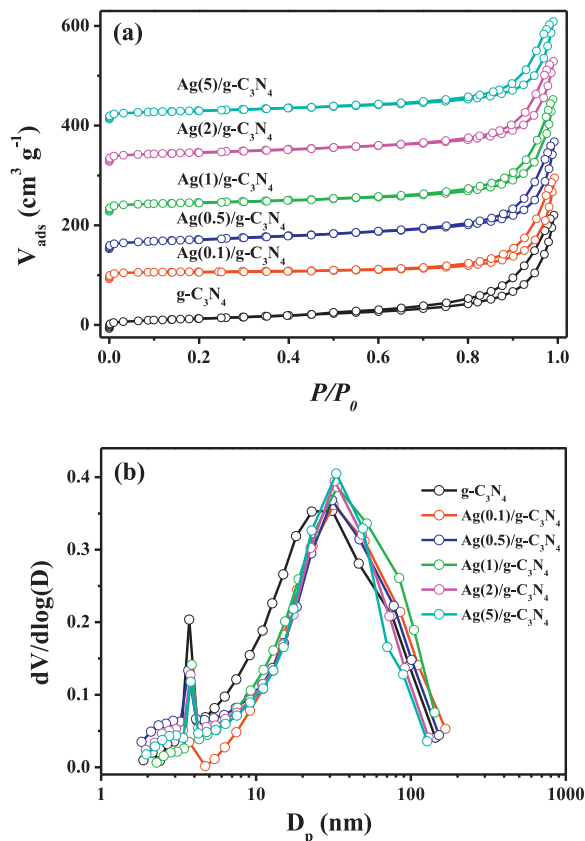


Fig. 4. Nitrogen gas adsorption–desorption isotherms (a) and BJH pore-size distribution curves (b) of g-C₃N₄ and Ag/g-C₃N₄ materials.

Ag(1)/g-C₃N₄, Ag(2)/g-C₃N₄ and Ag(5)/g-C₃N₄ are 68, 65, 64, 66 and 65 m² g⁻¹, respectively.

3.1.3. Morphology

The microstructures of as-prepared pure g-C₃N₄ and Ag/g-C₃N₄ (represented by Ag(2)/g-C₃N₄ and Ag(5)/g-C₃N₄) are revealed by TEM observations (Fig. 5). Pure g-C₃N₄ displays the platelet-like morphology that can be clearly seen in Fig. 5a. After deposition of silver particles on the g-C₃N₄, the platelet-like morphology remains intact; meanwhile, sphere-like silver particles homogeneously dispersed on the surface of g-C₃N₄ platelets (Fig. 5b and c). For Ag(2)/g-C₃N₄, the estimated particle size of the deposited Ag is ca. 10 nm (Fig. 5b). As for Ag(5)/g-C₃N₄, the particle size of the deposited Ag become large and uneven-distributed (10–100 nm), implying that some of Ag particles may aggregate into Ag clusters (Fig. 5c).

3.1.4. Optical absorption property

The light absorption property of as-prepared g-C₃N₄-based materials is studied by UV–vis/DRS, and the result is shown in Fig. 6. Pure g-C₃N₄ shows a typical semiconductor absorption in the region of 200–450 nm, originating from charge transfer response of g-C₃N₄ from the VB populated by N 2p orbitals to the CB formed by C 2p orbitals [18]. The estimated bandgap of the g-C₃N₄ is 2.7 eV, consistent with the literature results [18,46]. After deposition of Ag particles on the surface of g-C₃N₄, a new absorption peak appears in visible-light region (450–800 nm), and the absorbance of Ag/g-C₃N₄ increases gradually with Ag loading level from 0.1, 0.5, 1, 2, to 5 wt%. The new broad peak in the visible-light region is attributed to the characteristic SPR absorption of metallic silver particles, and therefore it is inferred that Ag(0.1)/g-C₃N₄ and Ag(5)/g-C₃N₄ shows

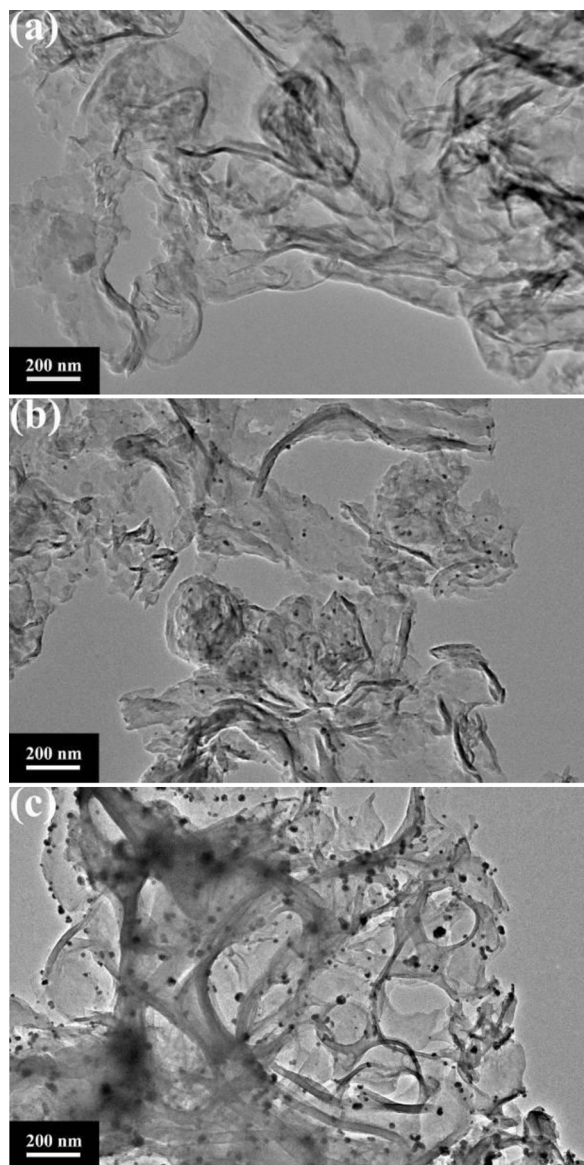


Fig. 5. TEM images of (a) $g\text{-C}_3\text{N}_4$, (b) $\text{Ag}(2)/g\text{-C}_3\text{N}_4$ and (c) $\text{Ag}(5)/g\text{-C}_3\text{N}_4$ materials.

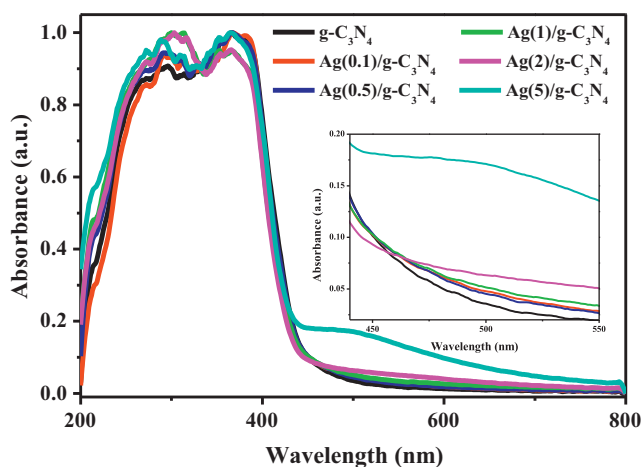


Fig. 6. UV-vis/DRS of $g\text{-C}_3\text{N}_4$ and $\text{Ag}/g\text{-C}_3\text{N}_4$ materials.

the weakest and strongest SPR effect among five tested $\text{Ag}/g\text{-C}_3\text{N}_4$ materials.

3.2. Photocatalytic studies

3.2.1. Visible-light photocatalytic activity

The photocatalytic activity of $g\text{-C}_3\text{N}_4$ and $\text{Ag}/g\text{-C}_3\text{N}_4$ materials is firstly evaluated by the degradation of dye MO (10 mg L^{-1} , 100 mL) under visible-light irradiation ($400\text{ nm} < \lambda < 680\text{ nm}$). For comparison, commercial photocatalyst, Degussa P25 TiO_2 , is also tested under the same conditions. MO is one of the most widely used dyes with stable azoic structure and weak adsorption on the photocatalyst surface, and therefore complete decomposition of MO is extremely difficult even by photocatalysis.

Fig. 7a shows the visible-light photocatalytic activity of $g\text{-C}_3\text{N}_4$ -based photocatalysts and P25 TiO_2 toward the degradation of MO. Before light irradiation, the adsorption behaviors of the tested photocatalysts are studied. It shows that the adsorption–desorption equilibrium between MO molecules and the photocatalyst reaches after stirring the suspension for 30 min, and the adsorption capacity of P25 TiO_2 , $g\text{-C}_3\text{N}_4$, $\text{Ag}(0.1)/g\text{-C}_3\text{N}_4$, $\text{Ag}(0.5)/g\text{-C}_3\text{N}_4$, $\text{Ag}(1)/g\text{-C}_3\text{N}_4$, $\text{Ag}(2)/g\text{-C}_3\text{N}_4$ and $\text{Ag}(5)/g\text{-C}_3\text{N}_4$ toward MO molecules is 14%, 13%, 13%, 15%, 17%, 21% and 35%, respectively. The result indicates that the adsorption ability of $\text{Ag}/g\text{-C}_3\text{N}_4$ enhances as increasing the Ag loading from 0.1 to 5 wt%, implying that the adsorption ability of $\text{Ag}/g\text{-C}_3\text{N}_4$ toward dye MO molecules is closely related to Ag nanoparticles. Considering the similar BET surface area of $\text{Ag}/g\text{-C}_3\text{N}_4$ materials with Ag loading from 0.1 to 5 wt%, it is inferred that the adsorption of $\text{Ag}/g\text{-C}_3\text{N}_4$ materials to MO molecules originates from Ag nanoparticles. From TEM results it has been clearly observed that more Ag particles appear for the $\text{Ag}/g\text{-C}_3\text{N}_4$ with higher Ag loading compared with $\text{Ag}/g\text{-C}_3\text{N}_4$ with lower Ag loading, and thereby the enhanced adsorption ability of the former to MO is obtained. Similar result has also been reported by other groups' work [47,48].

Additionally, in the absence of the photocatalyst, the decomposition of MO is negligible after visible-light irradiation for 120 min. However, significant degradation of MO occurs in the presence of both photocatalyst and visible-light irradiation, indicating that the disappearance of MO in current systems is mainly due to the generation, separation and transportation of the visible-light-induced charge carriers. Moreover, the photocatalytic activity of all tested $g\text{-C}_3\text{N}_4$ -based materials outperforms P25 TiO_2 , and $\text{Ag}/g\text{-C}_3\text{N}_4$ materials exhibit higher photocatalytic activity compared with pure $g\text{-C}_3\text{N}_4$, regardless of Ag loading levels. As for the $\text{Ag}/g\text{-C}_3\text{N}_4$ materials, their photocatalytic activity increases with Ag loading from 0.1% to 2 wt%, and further increasing Ag loading to 5 wt%, the photocatalytic activity remains unchangeable almost. For example, over period of 60 min visible-light irradiation, the conversion of MO reaches to 92% ($\text{Ag}(5)/g\text{-C}_3\text{N}_4$), 91% ($\text{Ag}(2)/g\text{-C}_3\text{N}_4$), 86% ($\text{Ag}(1)/g\text{-C}_3\text{N}_4$), 78% ($\text{Ag}(0.5)/g\text{-C}_3\text{N}_4$), 74% ($\text{Ag}(0.1)/g\text{-C}_3\text{N}_4$), 70% ($g\text{-C}_3\text{N}_4$) and 56% (P25 TiO_2), respectively.

It should be noted that the visible-light photocatalytic activity of P25 TiO_2 toward the degradation of MO is attributed to the photosensitized effect of dye, which has been widely studied by Zhao's group [1]. Under visible-light irradiation, dye MO molecules rather than TiO_2 is excited, which leads to electrons and MO^* . The produced electrons inject into the CB of TiO_2 , and then are further scavenged by O_2 to form $\cdot\text{O}_2^-$. Both MO^* and $\cdot\text{O}_2^-$ species are responsible for the decomposition of MO.

In order to exclude the photosensitized effect in the $\text{Ag}/g\text{-C}_3\text{N}_4$ -catalyzed organic pollutant degradation process, PNP, a light insensitive compound with light response in the UV region, is selected as the other target compound to further evaluate the visible-light photocatalytic activity of $\text{Ag}/g\text{-C}_3\text{N}_4$. Fig. 7b shows the visible-light photocatalytic activity of $g\text{-C}_3\text{N}_4$, $\text{Ag}(2)/g\text{-C}_3\text{N}_4$ and

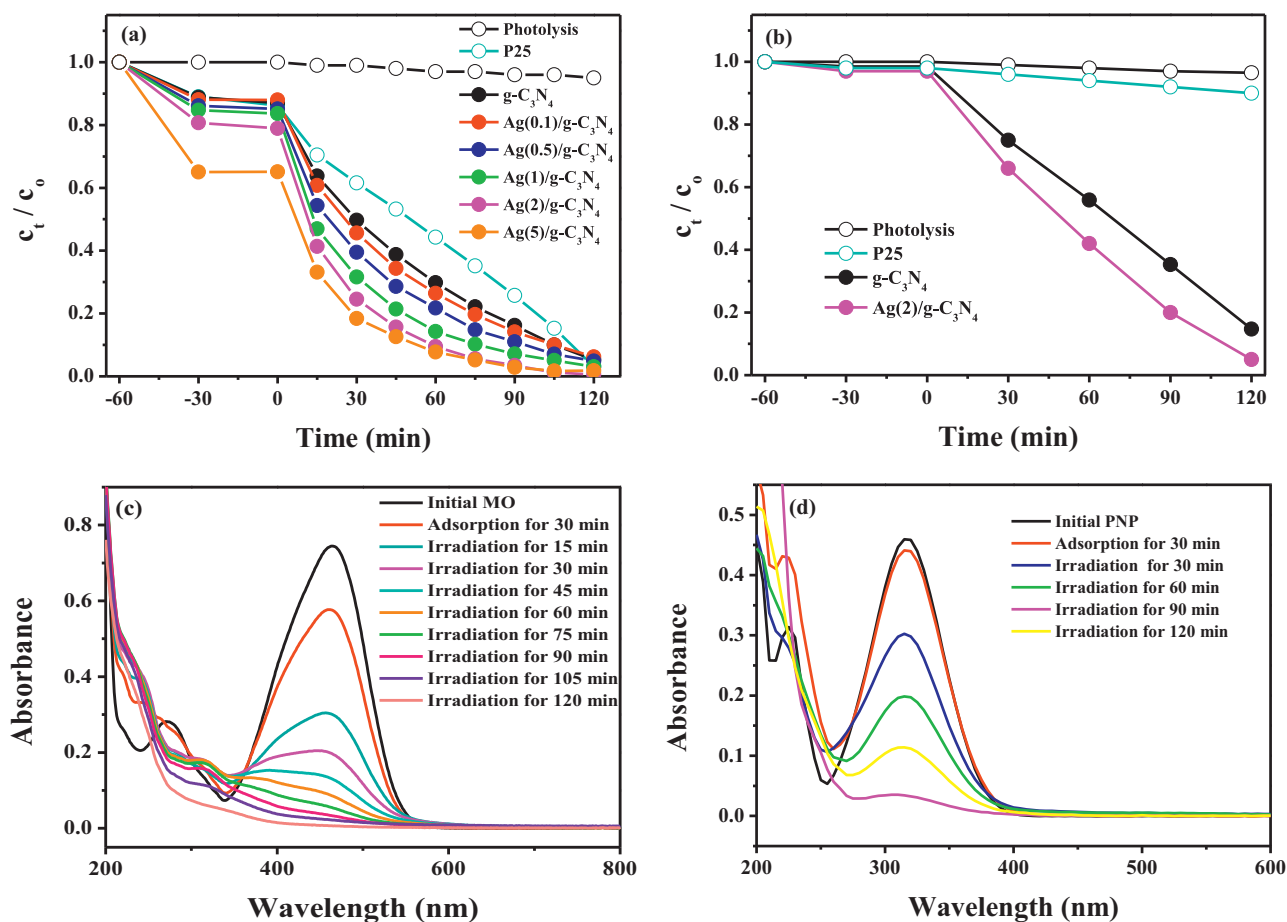


Fig. 7. Adsorption property and photocatalytic activity of g-C₃N₄ and Ag/g-C₃N₄ materials toward the degradation of (a) MO and (b) PNP under visible light irradiation (400 nm < λ < 680 nm). (c) and (d) are the UV-vis absorption spectra of MO (c) and PNP (d) solution as a function of irradiation time during the photocatalytic process over the Ag(2)/g-C₃N₄. Catalyst amount 100 mg; $c_0 = 10 \text{ mg L}^{-1}$; volume 100 mL.

P25 TiO₂ toward the degradation of PNP (10 mg L^{-1} , 100 mL). The blank experiments indicate that direct photolysis for 120 min or stirring the suspension of the catalyst and aqueous PNP in the dark for 30 min, the degradation of PNP is hardly occurred. However, significant degradation of PNP can be obtained after visible-light irradiating g-C₃N₄ and Ag(2)/g-C₃N₄. For instance, over period of 120 min visible-light irradiation, the conversion of PNP reaches to 98% for Ag(2)/g-C₃N₄ and 83% for g-C₃N₄. Under the same conditions, disappearance of PNP is lower than 10% by using P25 TiO₂ as the photocatalyst. The result further confirms that degradation of MO by visible-light irradiating TiO₂ is mainly due to the photosensitized effect rather than photocatalysis.

Fig. 7c and d shows the variations of the characteristic absorption of MO (at 464 nm) and PNP (at 317 nm) under visible-light irradiation by using Ag(2)/g-C₃N₄ as the photocatalyst. The characteristic absorptions of MO and PNP reduce gradually with prolonging the irradiation time, and the characteristic absorption of MO and PNP is hardly observed after 120 min visible-light irradiation. These results are consistent with those shown in Fig. 7a and b.

3.2.2. Mineralization ability

It is a crucial step to obtain total mineralization of aqueous organic pollutants during their photodecomposition processes since the yielded intermediates may be more toxic than the organic pollutant themselves. Generally, it takes much longer time to mineralize the organic pollutants totally compared with their degradation. Herein, the mineralization ability of as-prepared

Ag/g-C₃N₄ materials toward aqueous MO (10 mg L^{-1}) and PNP (10 mg L^{-1}) is evaluated by monitoring the concentrations of the final products (i.e., NO₃[−] and SO₄^{2−} for MO; NO₃[−] for PNP) in the reaction systems, and the most active Ag(2)/g-C₃N₄ is selected as the representative catalyst.

As for the mineralization of MO, the concentrations of NO₃[−] and SO₄^{2−} ions increase gradually with the visible-light irradiation time (Fig. 8a). For example, after 480 min visible-light irradiation, the concentrations of NO₃[−] and SO₄^{2−} are 1.2 and 2.0 mg L^{−1}, respectively, which are 21% and 69% of the expected concentration of NO₃[−] (5.6 mg L^{-1}) and SO₄^{2−} (2.9 mg L^{-1}). In the case of PNP, the expected concentration of NO₃[−] converted totally from 10 mg L^{-1} of PNP is 4.46 mg L^{-1} . From the result shown in Fig. 8b it can be seen that the yield of NO₃[−] ions reaches to 4.4 mg L^{-1} after 360 min visible-light irradiation, indicating complete conversion of PNP into the final product NO₃[−]. The above results indicate that as-prepared Ag/g-C₃N₄ can not only degrade aqueous MO and PNP but also mineralize them with the assistance of visible-light, working as the efficient photocatalysts to decompose of the organic pollutants in water.

3.2.3. Regeneration and reusability

For practical photocatalytic applications in aqueous solution, the recycling of the heterostructured photocatalyst systems is an important but difficult task owing to the leakage of the individual components during the photocatalytic procedures. Taking Ag(2)/g-C₃N₄ as the representative photocatalyst, the regeneration and reusability of as-prepared metallic silver deposited g-C₃N₄ material

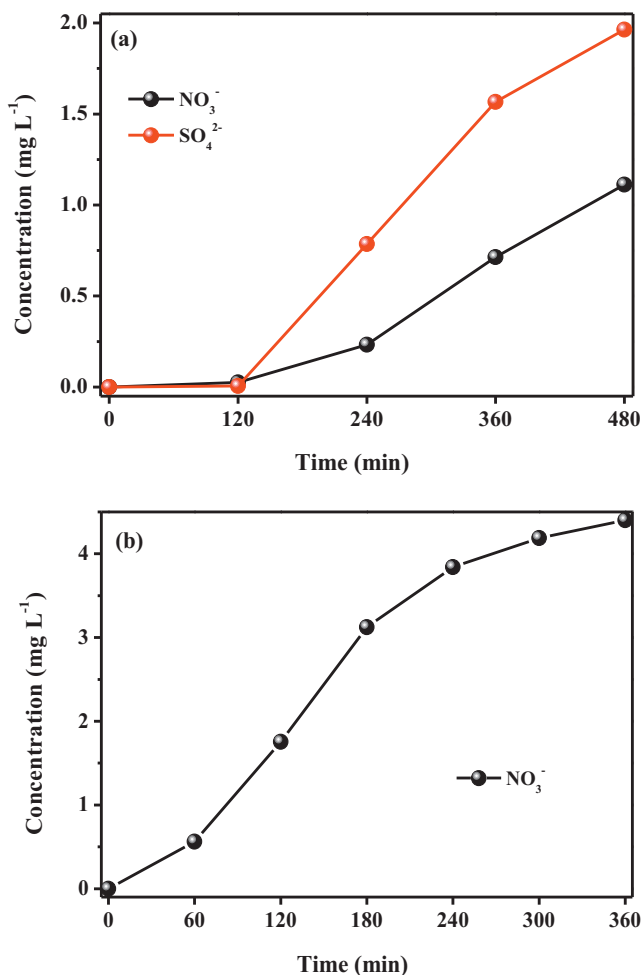


Fig. 8. Concentrations of the yielded NO₃⁻ and/or SO₄²⁻ ions in the Ag(2)/g-C₃N₄-photocatalyzed (a) MO and (b) PNP degradation system. Catalyst amount 100 mg; c₀ = 10 mg L⁻¹; volume 100 mL; 400 nm < λ < 680 nm.

is investigated by selecting dye MO as the target compound. For each recycling run, Ag(2)/g-C₃N₄ is collected by centrifugation, and then washed with ethanol at 60 °C for three times. As shown in Fig. 9, no apparent deactivation of the photocatalyst is observed after five consecutive runs, and the determined Ag leaching in the catalyst-free reaction system is 0.3%. Therefore,

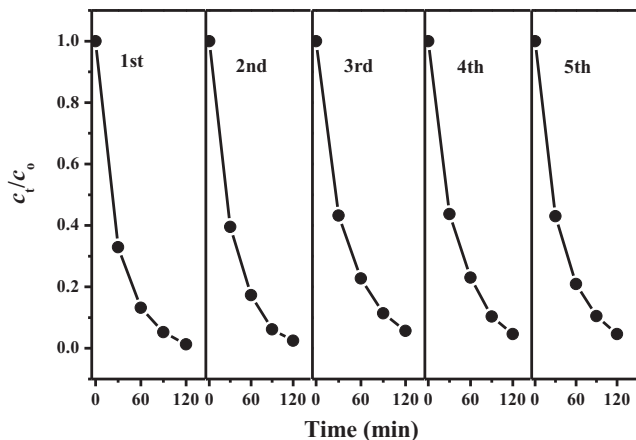


Fig. 9. Recycling experiments of visible-light photocatalytic degradation of dye MO over the Ag(2)/g-C₃N₄. Catalyst amount 100 mg; c₀ = 10 mg L⁻¹; volume 100 mL; 400 nm < λ < 680 nm.

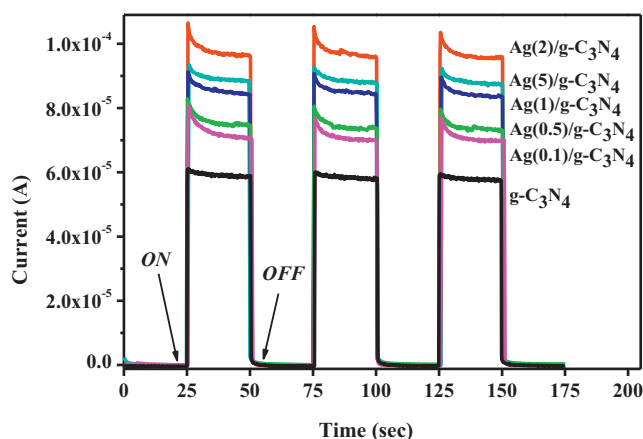


Fig. 10. Photocurrent responses of g-C₃N₄ and Ag/g-C₃N₄ electrodes in 0.01 mol L⁻¹ Na₂SO₄ electrolyte solution under Xe irradiation. The working electrode potential is constant at +1.0 V.

as-prepared Ag/g-C₃N₄ heterostructures show excellent catalytic stability, performing as genuine heterogeneous visible-light-driven photocatalysts to decompose aqueous organic pollutants effectively.

3.3. Mechanism considerations

3.3.1. Photoelectrochemical experiments

The generation of photoinduced electrons and holes as well as their separation, migration and capture by the reactive species is regarded as the basic process for the operation of semiconductor photocatalysts. Photoelectrochemistry test can provide a powerful tool to monitor these complicated processes. In current work, the photoelectrochemical properties of g-C₃N₄ and Ag/g-C₃N₄ are studied by using the g-C₃N₄/Ti or Ag/g-C₃N₄/Ti, Pt wire and Ag/AgCl (saturated KCl) as the working electrode, counter electrode and reference electrode, respectively, while Xe lamp is used as a light source. From the photocurrent–time (*I*–*t*) curves shown in Fig. 10 it can be seen that the sharp increased photocurrent responses appear for all tested working electrodes once the pulse Xe lamp irradiation is applied, and the generated photocurrents are reproducible and stable during three on-off intermittent irradiation cycles. Additionally, under the same conditions, all tested Ag/g-C₃N₄/Ti electrodes present higher photocurrent responses with respect to pure g-C₃N₄/Ti electrode; moreover, the photocurrent responses of Ag/g-C₃N₄/Ti electrodes increase gradually with the loading of Ag from 0.1, 0.5, 1, to 2 wt%, and then the photocurrent begins to decline. For the Ag(2)/g-C₃N₄/Ti electrode, it can produce the highest photocurrent intensity that is 1.7 times higher than that of pure g-C₃N₄/Ti electrode.

The prompt increase in photocurrent response from light-off to light-on state is mainly ascribed to the fast separation and transportation of the photogenerated e_{CB}⁻ on the surface of the working electrodes. Accordingly, it is inferred that Ag(2)/g-C₃N₄ and g-C₃N₄ exhibit the slowest and fastest e_{CB}⁻–h_{VB}⁺ recombination rate, respectively. Additionally, lower photocurrent response of Ag(5)/g-C₃N₄ with respect to Ag(2)/g-C₃N₄ indicates that the increased size and aggregation of Ag nanoparticles can induce new h_{VB}⁺–e_{CB}⁻ recombination center, and thereby prohibiting further generation of e_{CB}⁻ and h_{VB}⁺.

3.3.2. Photoluminescence measurements

Fig. 11 shows the room temperature PL spectra of g-C₃N₄ and Ag(2)/g-C₃N₄ under the excitation wavelength of 330 nm. The main emission peak is centered at ca. 460 nm for g-C₃N₄, which can be attributed to the band–band PL phenomenon with the energy of

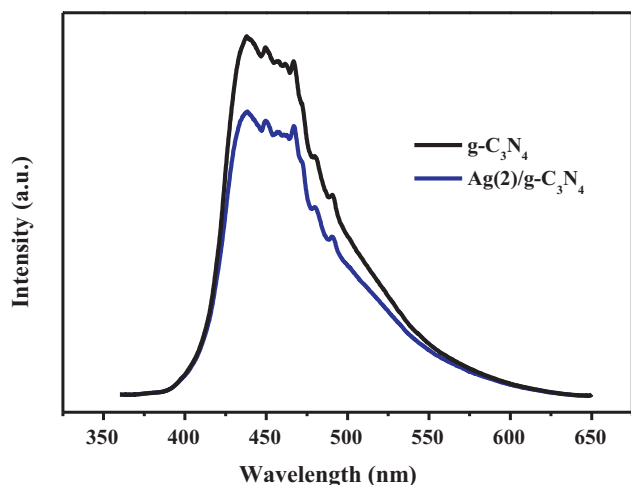


Fig. 11. Room temperature PL spectra of g-C₃N₄ and Ag(2)/g-C₃N₄ under the excitation wavelength of 330 nm.

light approximately equal to the band gap energy of g-C₃N₄ [45]. In the case of Ag(2)/g-C₃N₄, the position of the emission peak in PL spectrum is similar to that of g-C₃N₄, but the emission intensity significantly decreases. Considering that the PL emission results from the free charge carrier recombination, the decreased peak intensity indicates that Ag(2)/g-C₃N₄ exhibits slower $e_{CB}^- - h_{VB}^+$ recombination rate compared with pure g-C₃N₄ under the irradiation, which is consistent with the above photocurrent testing result.

3.3.3. Free radical and hole scavenging experiments

In order to understand the mechanism on the enhanced photocatalytic activity of the heterostructured Ag/g-C₃N₄ photocatalyst with respect to pure g-C₃N₄ in depth, the active species generated during the process of g-C₃N₄- and Ag(2)/g-C₃N₄-photocatalyzed PNP degradation are identified by free radical and hole trapping experiments. In this study, tert-butyl alcohol (*t*-BuOH), EDTA and 1,4-benzoquinone (BQ) are used as the hydroxyl radical (\cdot OH) scavenger, hole (h_{VB}^+) scavenger and superoxide radical (\cdot O₂⁻) scavenger, respectively [49,50].

Fig. 12a presents the influence of various scavengers on the visible-light photocatalytic activity of pure g-C₃N₄ toward the degradation of PNP. Compared with scavenger-free g-C₃N₄ photocatalytic system, the degradation rate of PNP is hardly inhibited after the addition of *t*-BuOH (1 mmol L⁻¹) in the reaction system. However, in the presence of EDTA (1 mmol L⁻¹), the degradation rate of PNP is decelerated obviously. As for the BQ (1 mmol L⁻¹)-g-C₃N₄ photocatalytic system, the degradation of PNP is inhibited greatly. The above results indicate that h_{VB}^+ is one of the active species generated in the g-C₃N₄-photocatalytic system, while \cdot O₂⁻ is the main active species that is responsible for the oxidation of PNP completely under the visible-light irradiation. As for \cdot OH radicals, it is hardly generated in current photocatalytic system.

Fig. 12b displays the influence of various scavengers on the visible-light photocatalytic activity of Ag/g-C₃N₄ heterostructure (represented by Ag(2)/g-C₃N₄) toward the degradation of PNP. It shows that \cdot O₂⁻ is still the main active species generated in current system since the degradation efficiency of PNP decreases significantly in the presence of BQ, while h_{VB}^+ is another active species that is responsible for the oxidation of PNP. Nevertheless, different from pure g-C₃N₄ photocatalytic system, the photodegradation of PNP over the Ag(2)/g-C₃N₄ can also be suppressed after the addition of *t*-BuOH in the reaction system. The above result indicates that \cdot OH radical is also the active species generated in the Ag/g-C₃N₄ photocatalytic system besides \cdot O₂⁻ radical and h_{VB}^+ species,

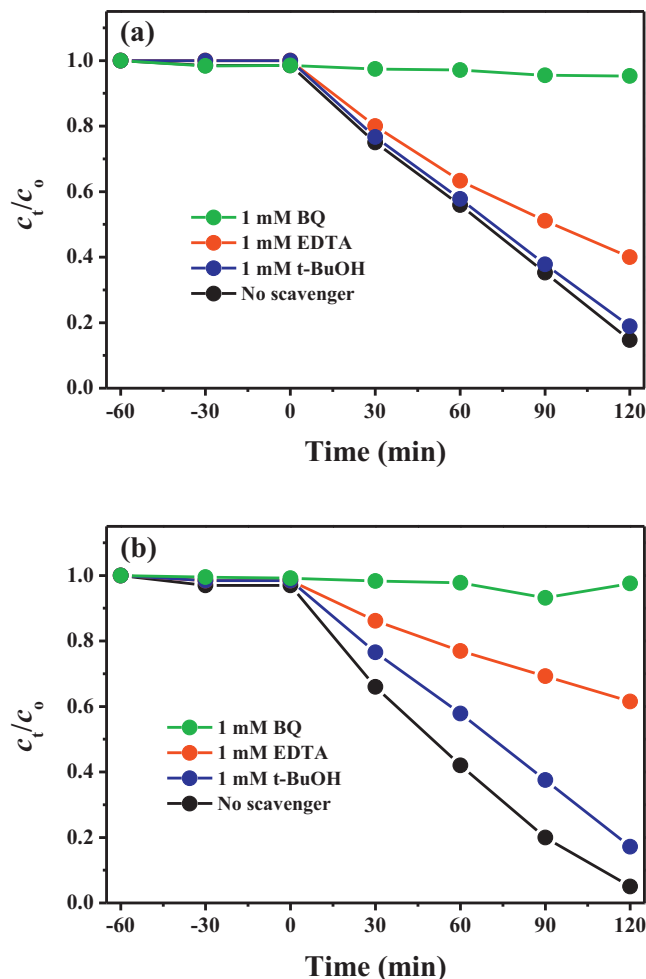
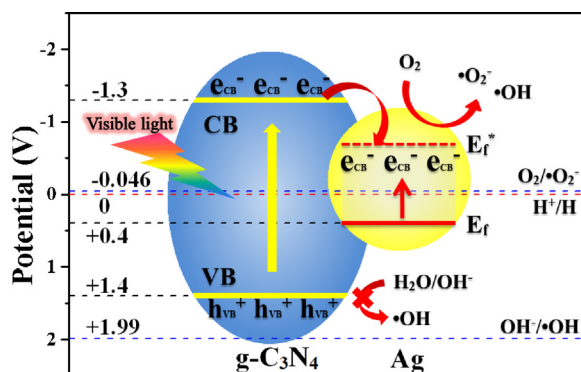


Fig. 12. Influence of various scavengers on the visible-light photocatalytic activity of (a) pure g-C₃N₄ and (b) Ag(2)/g-C₃N₄ toward the degradation of PNP. Catalyst amount 100 mg; $c_0 = 10 \text{ mg L}^{-1}$; volume 100 mL; $400 \text{ nm} < \lambda < 680 \text{ nm}$.

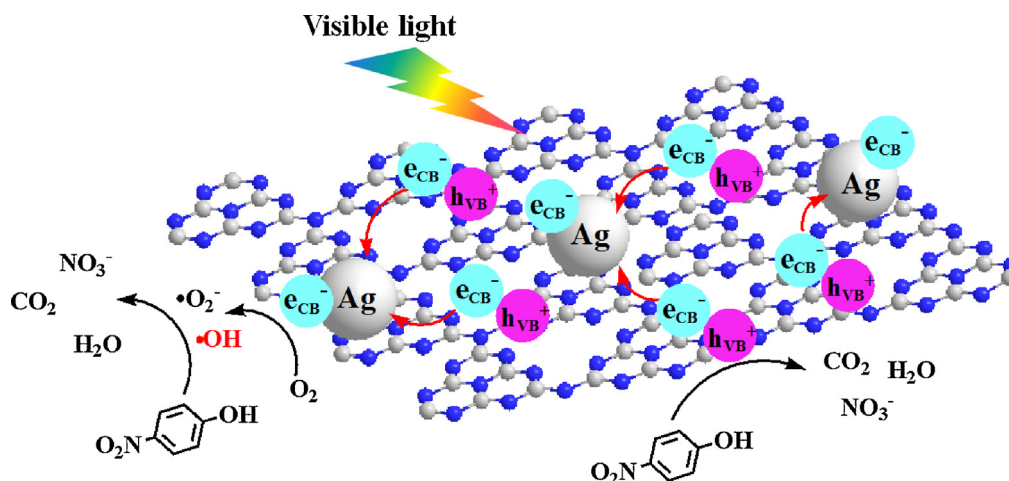
providing direct evidence for the enhanced photocatalytic activity of Ag/g-C₃N₄ with respect to g-C₃N₄ itself.

3.3.4. Discussion

On the basis of the related literature work and the above experimental results including physicochemical properties, photocatalytic properties, photoelectrochemical properties as well as the identified active species, it is inferred that the enhanced



Scheme 1. Generation, separation and transportation of h_{VB}^+ and e_{CB}^- at the interface of the visible-light-driven Ag/g-C₃N₄ plasmonic photocatalyst.



Scheme 2. Mechanism of visible-light photocatalytic degradation of aqueous PNP over the Ag/g-C₃N₄ plasmonic photocatalyst.

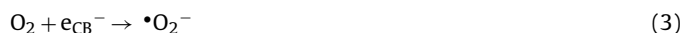
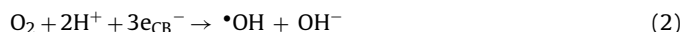
photocatalytic activity of g-C₃N₄ owing to the deposition of metallic silver nanoparticles is attributed to the following reasons.

On the one hand, the visible-light harvesting ability of Ag/g-C₃N₄ is enhanced due to SPR absorption of silver nanoparticles. Accordingly, more photoexcited carriers can be generated, giving a positive influence on the photocatalytic activity of the heterostructured Ag/g-C₃N₄. However, the photocatalytic activity of Ag(5)/g-C₃N₄ is almost the same as that of Ag(2)/g-C₃N₄ although the former shows much stronger SPR effect, suggesting that deposition of Ag nanoparticles with higher loading is unhelpful to further improve the photocatalytic activity of g-C₃N₄. One of the reasons is that the excess Ag nanoparticles may increase the light opacity, preventing g-C₃N₄ from the effective light absorption.

On the other hand, the fast generation of the photogenerated carriers on g-C₃N₄ and then rapid separation and transportation of these photogenerated carriers at the interface of g-C₃N₄ and Ag are the main reason for the enhanced visible-light photocatalytic activity of Ag/g-C₃N₄. The SPR effect of Ag nanoparticles can induce enhancement of the local electromagnetic field, which can speed the generation rate of e_{CB}^- and h_{VB}^+ within g-C₃N₄ [39]. Additionally, Ag and g-C₃N₄ possess the matched energy levels (Scheme 1). The theoretical calculated CB and VB potential of g-C₃N₄ are −1.3 and 1.4 V (vs. NHE) [46], respectively, while the Fermi level of Ag is 0.4 V (vs. NHE) [38]. After visible-light irradiating, the generated e_{CB}^- on g-C₃N₄ can be scavenged rapidly by Ag nanoparticles, creating a Schottky barrier that minimizes the recombination of e_{CB}^- and h_{VB}^+ . The above explanation is evidenced by the photoelectrochemical and PL testing results. Nevertheless, at Ag loading of 5%, the increased particle size and aggregation of Ag may produce new charge recombination center, which limits the further improvement of the photocatalytic activity of Ag/g-C₃N₄ [51,52].

After the separation of e_{CB}^- and h_{VB}^+ , these two kind of photogenerated charge carriers would be transferred into the active species (e.g., h_{VB}^+ , $\bullet O_2^-$, and/or $\bullet OH$) that are responsible for the degradation and mineralization of MO or PNP in aqueous solution. Compared the VB potential of g-C₃N₄ with the standard redox potential of $OH^-/\bullet OH$ (Scheme 1) it is found that the VB potential of g-C₃N₄ is more negative than the standard redox potential of $OH^-/\bullet OH$ (1.99 V vs. NHE), and therefore h_{VB}^+ cannot oxidize OH^- to generate $\bullet OH$ radicals directly in pure g-C₃N₄ photocatalytic system (Eq. (1)). However, in Ag/g-C₃N₄ heterostructure system, the effective separation of e_{CB}^- and h_{VB}^+ owing to the introduction of metallic Ag nanoparticles can provide e_{CB}^- with sufficient time to participate in the multiple-electron reduction reaction of oxygen, leading to the generation of $\bullet OH$ radicals indirectly (Eq. (2)) [41,53]. This is the direct reason for the enhanced photocatalytic activity of

Ag/g-C₃N₄ with respect to pure g-C₃N₄. Additionally, with the e_{CB}^- of g-C₃N₄ injecting into the Fermi level of Ag nanoparticles, the Ag Fermi level shifts from 0.4 V (vs. NHE) to the energy level higher than the standard redox potential of $O_2/\bullet O_2^-$ (−0.046 V vs. NHE), leading to a reserved reduction ability of e_{CB}^- for the formation of $\bullet O_2^-$ radicals (Eq. (3)).



On the basis of the above discussion, a reasonable mechanism of visible-light photocatalytic degradation of PNP over the heterostructured Ag/g-C₃N₄ is revealed and illustrated in Scheme 2. Under visible-light irradiation, e_{CB}^- and h_{VB}^+ are generated on the surface of g-C₃N₄. Due to the matched energy levels of Ag and g-C₃N₄, e_{CB}^- can transfer to Ag nanoparticles rapidly, leaving the h_{VB}^+ located on the VB of g-C₃N₄. Subsequently, the transferred e_{CB}^- on Ag nanoparticles react with O_2 to produce $\bullet O_2^-$ and $\bullet OH$ radicals. These oxidative species including $\bullet O_2^-$, $\bullet OH$ and h_{VB}^+ are responsible for the complete degradation of PNP to NO_3^- , H_2O and CO_2 .

4. Conclusions

An efficient visible-light plasmonic photocatalyst, Ag/g-C₃N₄ heterostructure, is facily fabricated by a simple polymerization–photodeposition route. Compared with pure g-C₃N₄, the enhanced photocatalytic activity of Ag/g-C₃N₄ toward the degradation of MO and PNP is explained by the enhanced visible-light utilization efficiency due to the SPR absorption of silver nanoparticles as well as fast generation, separation and transportation of the photogenerated carriers. In pure g-C₃N₄-based visible-light system, $\bullet O_2^-$ and h_{VB}^+ are identified as the active species that are responsible for the degradation of the target pollutants. In Ag/g-C₃N₄-based visible-light system, besides $\bullet O_2^-$ and h_{VB}^+ species, $\bullet OH$ radical is also found to participate in the target reactions, providing the direct evidence to account for the enhanced photocatalytic activity of Ag/g-C₃N₄. In addition, Ag/g-C₃N₄ heterostructure exhibits enough catalytic stability, performing as genuine heterogeneous visible-light-driven photocatalyst to decompose aqueous organic pollutants effectively.

Acknowledgments

This work was supported by the Natural Science Fund Council of China (21173036; 51178092; 51278092; 51238001), the Fundamental Research Funds for the Central Universities (12SSXT148; 11SSXT135), the Science and Technology Project of Jilin Province (20086035), and Northeast Normal University Postdoctoral Fund.

References

- [1] C.C. Chen, W.H. Ma, J.C. Zhao, *Chemical Society Reviews* 39 (2010) 4206–4219.
- [2] G. Liu, L.Z. Wang, H.G. Yang, H.M. Cheng, G.Q. Lu, *Journal of Materials Chemistry* 20 (2010) 831–843.
- [3] D.Q. Zhang, G.S. Li, J.C. Yu, *Journal of Materials Chemistry* 20 (2010) 4529–4536.
- [4] M.D. Hernandez-Alonso, F. Fresno, S. Suarez, J.M. Coronado, *Energy and Environmental Science* 2 (2009) 1231–1257.
- [5] H. Tong, S. Ouyang, Y. Bi, N. Umezawa, M. Oshikiri, J. Ye, *Advanced Materials* 24 (2012) 229–251.
- [6] M.L. de Souza, P. Corio, *Applied Catalysis B: Environmental* 136/137 (2013) 325–333.
- [7] M. Radoičić, Z. Šaponjić, I.A. Janković, G. Ćirić-Marjanović, S.P. Ahrenkiel, M.I. Comor, *Applied Catalysis B: Environmental* 136/137 (2013) 133–139.
- [8] M.B. Radoičić, I.A. Janković, V.N. Despotović, D.V. Šojić, T.D. Savić, Z.V. Šaponjić, B.F. Abramović, M.I. Comor, *Applied Catalysis B: Environmental* 138/139 (2013) 122–127.
- [9] J.X. Wang, P.X. Wang, Y.T. Cao, J. Chen, W.J. Li, Y. Shao, Y. Zheng, D.Z. Li, *Applied Catalysis B: Environmental* 136/137 (2013) 94–102.
- [10] T.T. Li, Y.M. He, H.J. Lin, J. Cai, L.Z. Dong, X.X. Wang, M.F. Luo, L.H. Zhao, X.D. Yi, W.Z. Weng, *Applied Catalysis B: Environmental* 138/139 (2013) 95–103.
- [11] W.D. Shi, J.Q. Shi, S. Yu, P. Liu, *Applied Catalysis B: Environmental* 138/139 (2013) 184–190.
- [12] D.G. Wang, H.F. Jiang, X. Zong, Q. Xu, Y. Ma, G.L. Li, C. Li, *Chemistry: A European Journal* 17 (2011) 1275–1282.
- [13] Y.N. Guo, L. Chen, X. Yang, F.Y. Ma, S.Q. Zhang, Y.X. Yang, Y.H. Guo, X. Yuan, *RSC Advances* 2 (2012) 4656–4663.
- [14] D.Q. He, L.L. Wang, D.D. Xu, J.L. Zhai, D.J. Wang, T.F. Xie, *ACS Applied Materials & Interfaces* 3 (2011) 3167–3171.
- [15] K. Maeda, *Physical Chemistry Chemical Physics* (2013), <http://dx.doi.org/10.1039/C2CP43914J>.
- [16] B. Siritanaratkul, K. Maeda, T. Hisatomi, K. Domen, *ChemSusChem* 4 (2011) 74–78.
- [17] J.G. Hou, Z. Wang, W.B. Kan, S.Q. Jiao, H.M. Zhu, R.V. Kumar, *Journal of Materials Chemistry* 22 (2012) 7291–7299.
- [18] X.C. Wang, K. Maeda, A. Thomas, K. Takanabe, G. Xin, J.M. Carlsson, K. Domen, M. Antonietti, *Nature Materials* 8 (2009) 76–80.
- [19] K. Takanabe, K. Kamata, X. Wang, M. Antonietti, J. Kubota, K. Domen, *Physical Chemistry Chemical Physics* 12 (2010) 13020–13025.
- [20] Y.W. Zhang, J.H. Liu, G. Wu, W. Chen, *Nanoscale* 4 (2012) 5300–5303.
- [21] G.G. Zhang, J.S. Zhang, M.W. Zhang, X.C. Wang, *Journal of Materials Chemistry* 22 (2012) 8083–8091.
- [22] J.S. Zhang, M.W. Zhang, R.Q. Sun, X.C. Wang, *Angewandte Chemie International Edition* 51 (2012) 10145–10149.
- [23] S.C. Yan, Z.S. Li, Z.G. Zou, *Langmuir* 26 (2010) 3894–3901.
- [24] S.C. Yan, Z.S. Li, Z.G. Zou, *Langmuir* 25 (2009) 10397–10401.
- [25] Y.J. Wang, Z.X. Wang, S. Muhammad, J. He, *CrystEngComm* 14 (2012) 5065–5070.
- [26] J.D. Hong, X.Y. Xia, Y.S. Wang, R. Xu, *Journal of Materials Chemistry* 22 (2012) 15006–15012.
- [27] F. Dong, L.W. Wu, Y.J. Sun, M. Fu, Z.B. Wu, S.C. Lee, *Journal of Materials Chemistry* 21 (2011) 15171–15174.
- [28] B. Chai, T.Y. Peng, J. Mao, K. Li, L. Zan, *Physical Chemistry Chemical Physics* 14 (2012) 16745–16752.
- [29] J.H. Liu, Y.W. Zhang, L.H. Lu, G. Wu, W. Chen, *Chemical Communications* 48 (2012) 8826–8828.
- [30] Y.J. Wang, R. Shi, J. Lin, Y.F. Zhu, *Energy & Environmental Science* 4 (2011) 2922–2929.
- [31] J.X. Sun, Y.P. Yuan, L.G. Qiu, X. Jiang, A.J. Xie, Y.H. Shen, J.F. Zhu, *Dalton Transactions* 41 (2012) 6756–6763.
- [32] S. Ye, L.G. Qiu, Y.P. Yuan, Y.J. Zhu, J. Xia, J.F. Zhu, *Journal of Materials Chemistry A* 1 (2013) 3008–3015.
- [33] L.M. Sun, X. Zhao, C.J. Jia, Y.X. Zhou, X.F. Cheng, P. Li, L. Liu, W.L. Fan, *Journal of Materials Chemistry* 22 (2012) 23428–23438.
- [34] Y.J. Wang, X.J. Bai, C.S. Pan, J. He, Y.F. Zhu, *Journal of Materials Chemistry* 22 (2012) 11568–11573.
- [35] J. Fu, Y.L. Tian, B.B. Chang, F.N. Xi, X.P. Dong, *Journal of Materials Chemistry* 22 (2012) 21159–21166.
- [36] T.T. Li, L.H. Zhao, Y.M. He, J. Cai, M.F. Luo, J.J. Lin, *Applied Catalysis B: Environmental* 129 (2013) 255–263.
- [37] H. Xu, J. Yan, Y.G. Xu, Y.H. Song, H.M. Li, J.X. Xia, C.J. Huang, H.L. Wan, *Applied Catalysis B: Environmental* 129 (2013) 182–193.
- [38] J.T. Li, S.K. Cushing, J. Bright, F.K. Meng, T.R. Senty, P. Zheng, A.D. Bristow, N.Q. Wu, *ACS Catalysis* 3 (2012) 47–51.
- [39] D.B. Ingram, P. Christopher, J.L. Bauer, S. Linic, *ACS Catalysis* 1 (2011) 1441–1447.
- [40] S.W. Cao, Z. Yin, J. Barber, F.Y.C. Boey, S.C.J. Loo, C. Xue, *ACS Applied Materials & Interfaces* 4 (2011) 418–423.
- [41] Y.P. Bi, H.Y. Hu, S.X. Ouyang, Z.B. Jiao, G.X. Lu, J.H. Ye, *Journal of Materials Chemistry* 22 (2012) 14847–14850.
- [42] J.H. Liu, T.K. Zhang, Z.C. Wang, G. Dawson, W. Chen, *Journal of Materials Chemistry* 21 (2011) 14398–14401.
- [43] P. Niu, G. Liu, H.M. Cheng, *Journal of Materials Chemistry C* 116 (2012) 11013–11018.
- [44] X.G. Li, M.R. Huang, S.X. Li, *Acta Materialia* 52 (2004) 5363–5374.
- [45] L. Ge, C. Han, *Applied Catalysis B: Environmental* 117/118 (2012) 268–274.
- [46] X.C. Wang, S. Blechert, M. Antonietti, *ACS Catalysis* 2 (2012) 1596–1606.
- [47] Y. Li, G. Lu, S. Li, *Journal of Photochemistry and Photobiology A* 152 (2002) 219–228.
- [48] A.V. Rupa, D. Manikandan, D. Divakar, T. Sivakumar, *Journal of Hazardous Materials* 147 (2007) 906–913.
- [49] C.S. Pan, Y.F. Zhu, *Environmental Science and Technology* 44 (2010) 5570–5574.
- [50] C.C. Chen, Q. Wang, P.X. Lei, W.J. Song, W.H. Ma, J.C. Zhao, *Environmental Science and Technology* 40 (2006) 3965–3970.
- [51] X. Yang, Y.H. Wang, L.L. Xu, X.D. Yu, Y.H. Guo, *Journal of Physical Chemistry C* 112 (2008) 11481–11489.
- [52] Y.X. Yang, F. Su, S.Q. Zhang, W. Guo, X. Yuan, Y.H. Guo, *Colloids and Surfaces A* 415 (2012) 399–405.
- [53] G.H. Jiang, R.J. Wang, X.H. Wang, X.G. Xi, R.B. Hu, Y. Zhou, S. Wang, T. Wang, W.X. Chen, *ACS Applied Materials & Interfaces* 4 (2012) 4440–4444.